nature nanotechnology

ARTICLES

https://doi.org/10.1038/s41565-021-00881-9

Check for updates

Electrically reconfigurable non-volatile metasurface using low-loss optical phase-change material

Yifei Zhang[1], Clayton Fowler[2], Junhao Liang[1], Bilal Azhar[1], Mikhail Y. Shalaginov[1], Skylar Deckoff-Jones[1], Sensong An[2], Jeffrey B. Chou[3], Christopher M. Roberts[3], Vladimir Liberman[3], Myungkoo Kang[4], Carlos Ríos[1], Kathleen A. Richardson[4], Clara Rivero-Baleine[5], Tian Gu[1,6], Hualiang Zhang[2] ✉ and Juejun Hu[1,6] ✉

Active metasurfaces promise reconfigurable optics with drastically improved compactness, ruggedness, manufacturability and functionality compared to their traditional bulk counterparts. Optical phase-change materials (PCMs) offer an appealing material solution for active metasurface devices with their large index contrast and non-volatile switching characteristics. Here we report a large-scale, electrically reconfigurable non-volatile metasurface platform based on optical PCMs. The optical PCM alloy used in the devices, $Ge_2Sb_2Se_4Te$ (GSST), uniquely combines giant non-volatile index modulation capability, broadband low optical loss and a large reversible switching volume, enabling notably enhanced light–matter interactions within the active optical PCM medium. Capitalizing on these favourable attributes, we demonstrated quasi-continuously tuneable active metasurfaces with record half-octave spectral tuning range and large optical contrast of over 400%. We further prototyped a polarization-insensitive phase-gradient metasurface to realize dynamic optical beam steering.

Metasurfaces, planar electromagnetic artificial media comprising arrays of subwavelength-scale antennas or 'meta atoms', have been widely regarded as a promising platform enabling optical elements with substantial potential size, weight, power and cost benefits over their conventional bulk counterparts. Active metasurfaces, whose optical responses can be dynamically modulated, further enable exciting opportunities for agile manipulation of light propagation and interaction with matter[1–3]. So far, active tuning of metasurfaces has leveraged mechanical deformation[4,5], electrochemical or chemical reactions[6], electro-optic[7–10] and thermo-optic effects[11], as well as phase-change media[12–25]. In particular, phase-change materials (PCMs) based on chalcogenide alloys are uniquely poised for realizing phase-gradient active metasurfaces, since the giant refractive index contrast imparted by their structural transition facilitates broad optical phase tuning[26]. For instance, we have recently demonstrated that full 2π phase coverage can be achieved in PCM-based active metasurfaces, enabling binary switching between arbitrary phase profiles[27,28].

So far, active modulation of PCM-based metasurfaces has relied on thermal annealing[19,20,27,29–32] or optical writing[22–25,33,34]. These modulation schemes, however, necessitate bulky heating furnaces or ultrafast lasers. Electrical switching of PCM, on the other hand, is naturally conducive to compact integration with flat optics and foresees miniaturized, chip-scale reconfigurable optical systems. While electrical addressing of PCM is already a mature technology in phase-change random-access memories, the much larger device area essential for optical devices—as compared to today's deeply scaled phase-change random-access memories—places more stringent requirements on switching homogeneity across large areas. This technical challenge is epitomized by the phenomenon of filamentation: a thin wire of PCM that initially crystallizes becomes an electrical current conduit with substantially higher conductivity than the surrounding amorphous matrix, preventing uniform crystallization of the entire PCM volume. Filamentation precludes switching by passing current directly through PCM[26]. To address this challenge, we report in this work a large-area, reconfigurable metasurface based on electrothermal switching of PCM. Our work advances the state-of-the-art in three important aspects. First, our devices are made of a recently developed PCM, $Ge_2Sb_2Se_4Te$ or GSST[35–37]. Compared to the prevailing GeSbTe alloys, GSST offers two unique advantages specific to active metasurfaces: its broadband transparency across different structural states mitigates optical losses, and its much larger switching volume allows for optically thick PCM structures to boost light-PCM interactions while maintaining dynamic and fully reversible switching capacity[23,37]. The latter feature underpins the giant optical contrast and tuning range of our devices. Second, we have demonstrated voltage-controlled multi-state tuning of the PCM metasurface covering a record half-octave spectral regime. While multi-state operation has been reported in PCM-integrated waveguide devices[38–41], we show that progressive phase transition in our devices proceeds in a distinctively different, spatially uniform manner facilitating precise meta-atom tuning. Last but not least, we have realized large-area (up to $0.4 \times 0.4\,mm^2$), uniform electrothermal switching of PCMs

[1]Department of Materials Science and Engineering, Massachusetts Institute of Technology, Cambridge, MA, USA. [2]Department of Electrical and Computer Engineering, University of Massachusetts Lowell, Lowell, MA, USA. [3]Lincoln Laboratory, Massachusetts Institute of Technology, Lexington, MA, USA. [4]The College of Optics and Photonics, Department of Materials Science and Engineering, University of Central Florida, Orlando, FL, USA. [5]Missiles and Fire Control, Lockheed Martin Corporation, Orlando, FL, USA. [6]Materials Research Laboratory, Massachusetts Institute of Technology, Cambridge, MA, USA. ✉e-mail: hualiang_zhang@uml.edu; hujuejun@mit.edu

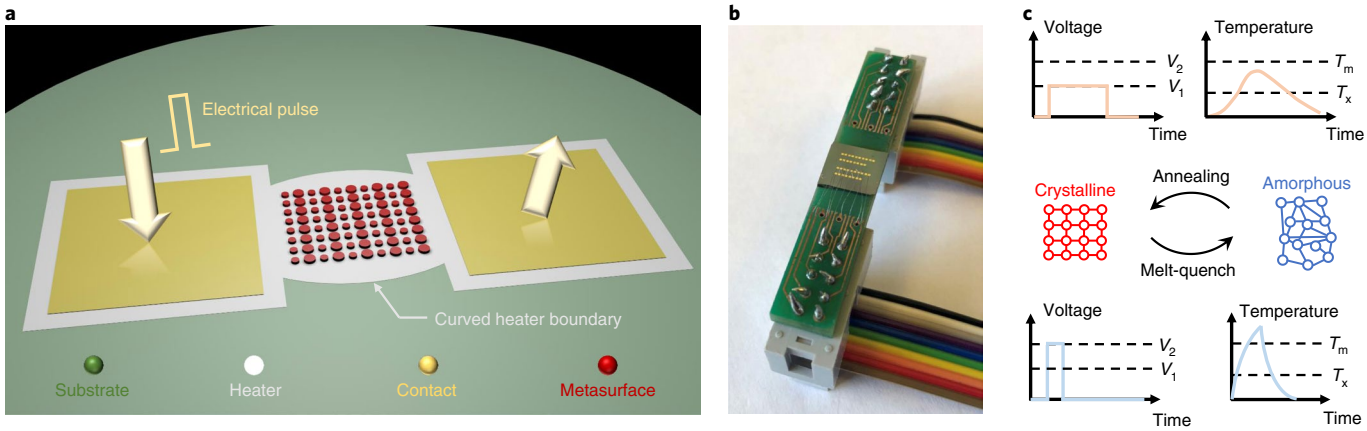

Fig. 1 | Device configuration and switching schemes. a, Schematic rendering showing the electrothermal metasurface switching configuration. **b**, Photo of a packaged metasurface array device, wire bonded onto a custom-designed PCB. **c**, Electrical pulsing schemes and meta-atom temperature profiles during (top) crystallization and (bottom) amorphization cycles, where T_m and T_x denote melting point and crystallization temperature of GSST, respectively, and V_1 and V_2 denote crystallization voltage and amorphization voltage, respectively.

using geometrically optimized heaters, which heralds topologically optimized heater designs towards ultimate scaling of active metasurface aperture size.

Electrothermal switching device platform

Each electrically reconfigurable metasurface device comprises meta atoms resting on a metal heater, which also acts as a reflector (Fig. 1a). The meta atoms are patterned in a GSST film and the fabrication process details are described in Methods. The metasurface device arrays were then wire bonded to a printed circuit board (PCB) carrier with pluggable ribbon cable connections to facilitate computerized control of the devices (Fig. 1b). In each device, the structural state of the meta atoms is collectively controlled by electrical pulsing, where a long, low-voltage (500 ms duration, <12 V) pulse triggers crystallization via Joule heating, whereas a short, high-voltage (5 µs, 20–23 V) pulse re-amorphizes the meta atoms via a melt-quench process (Fig. 1c).

PCM metasurfaces with square apertures of varying sizes (from 0.1×0.1 to $0.4\times0.4\,mm^2$) were fabricated. Compared to previously reported electrothermal PCM switching devices[37,42,43], the heater unit area reported here is more than two orders of magnitude larger. Mitigation of thermal non-uniformity becomes a critical challenge with enlarged metasurface aperture size, since large temperature excursions (1) preclude precise multi-state tuning due to non-uniform switching during crystallization and (2) compromise device reliability owing to emergence of 'hot spots' during amorphization. To illustrate this challenge, Fig. 2a plots the simulated steady-state temperature profile during a crystallization pulse for a classical square-shaped heater within the 0.15-mm device aperture. It is apparent that temperature near the perimeter of the aperture is considerably lower due to more efficient heat dissipation. To counter the issue, we introduced curved heater boundaries (Fig. 1a) to both lower current density in the heater centre and move the heater boundary further away from the metasurface aperture. Figure 2b presents the corresponding temperature profile for a heater with optimized boundary curvature (Supplementary Information) showing substantially improved in-plane uniformity. On the basis of the optimized heater design, Fig. 2c maps the average heater temperature for different pulse duration and voltage combinations that successfully amorphized/crystallized the devices in experiments, and the results (550–630 K for crystallization indicated by the light blue line, 1,020 K for amorphization indicated by the dark blue point) are in excellent agreement with our previous data[37,44].

We further investigated thermal uniformity inside meta atoms along the out-of-plane (through-thickness) direction. Figure 2d plots the temperature distributions along the out-of-plane direction for different time durations after onset of the electrical pulse, all normalized to the respective peak temperature at the heater surface. Within 5 µs (duration of the amorphization pulse), the temperature distribution has approached the steady state with an average temperature deviation of only 4 K throughout the entire meta atom. The negligible temperature gradient in the meta atoms, coupled with the reduced temperature sensitivity of crystallization kinetics in PCMs at temperatures well above glass transition[45], indicates that the transition proceeds progressively and uniformly throughout the meta atoms during crystallization, leading to a mixture of interspersed crystalline and amorphous phases. This contrasts with intermediate states of PCM elements integrated with waveguide devices, where the crystalline and amorphous phases are spatially localized[39]. The meta-atom tuning mechanism is viable since GSST is classified as a nucleation-dominated PCM[37], such that GSST nanocrystals can precipitate and grow from an amorphous matrix throughout the meta-atom volume. The ability to precisely access different intermediate states with voltage control is critical to enabling multi-state operation of the PCM active metasurface, a key attribute of our strategy.

Active metasurface characterization

Figure 3a depicts an archetypal metasurface consisting of a periodic array of identical GSST meta atoms. The meta-atom dimensions are chosen such that the meta atoms support two distinctive hybrid plasmonic-photonic modes (Fig. 3b inset (1) and (3), details can be found in Supplementary Information) in their amorphous and crystalline states in the target wavelength range. Evident from the simulated spectra in Fig. 3b, switching between the two states creates a large optical contrast at 1.49 µm wavelength, where efficient coupling to mode 1 in the crystalline state occurs while coupling to mode 3 in the amorphous state is suppressed due to optical phase mismatch.

The design principle is validated by our experimental data in Fig. 3c showing the reflectance spectra of the device after 40 crystallization–amorphization switching cycles. Complete reversible switching of the GSST material is also verified using micro-Raman measurements (Supplementary Information). The device boasts a large absolute optical reflectance (ΔR) contrast of 40% at 1.49 µm wavelength and a relative reflectance modulation ($\Delta R/R$) up to 400% at a

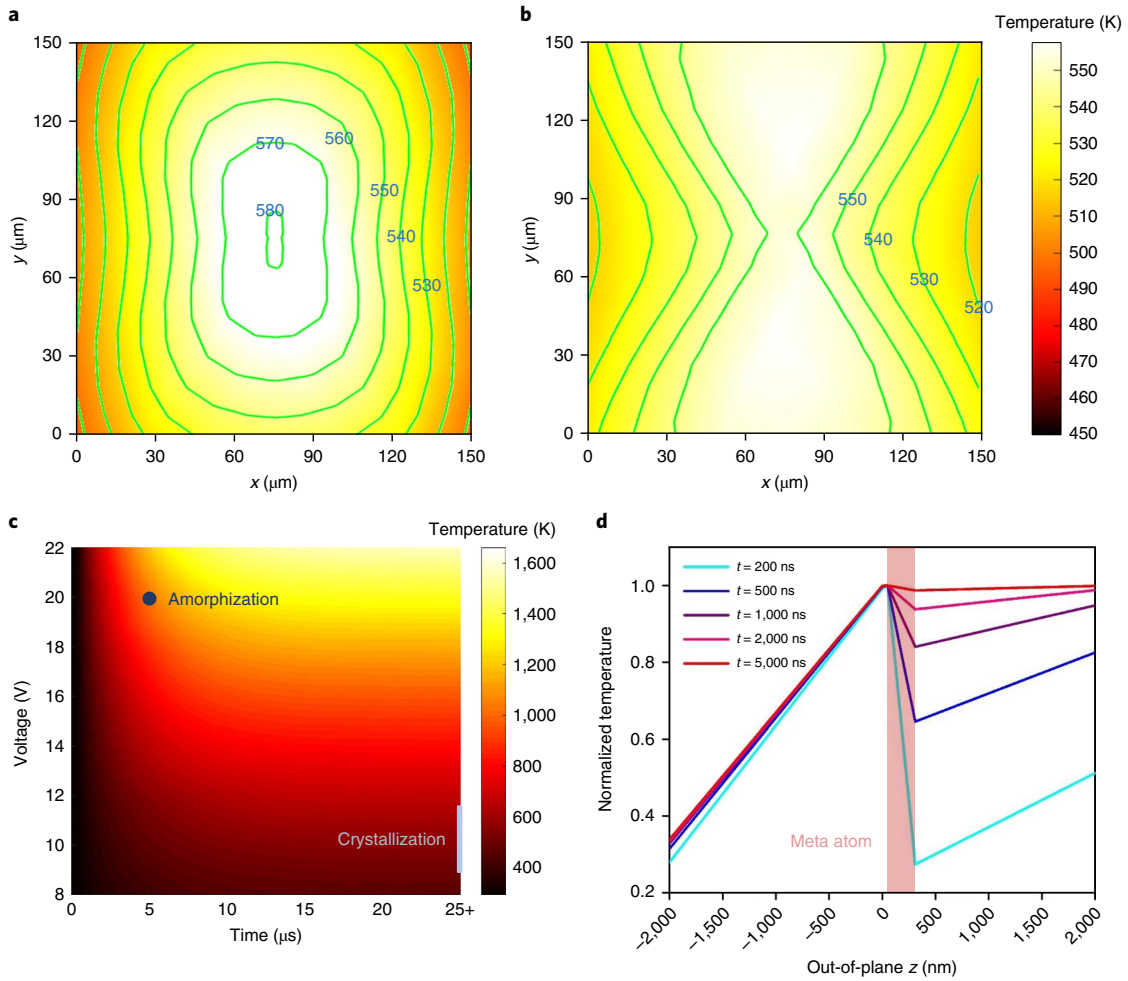

Fig. 2 | Temperature distribution of the device platform. a,**b**, Simulated steady-state temperature profiles within the metasurface aperture on the surfaces of a classical square-shaped heater (**a**) and an optimized heater with curved boundaries (**b**). **c**, Average heater temperature for different pulse duration and voltage combinations; the experimental parameters corresponding to amorphization and crystallization pulses are also labelled. **d**, Normalized temperature distributions along the out-of-plane direction for different time durations after onset of the pulse; the colour bar marks the position of the PCM meta-atom layer.

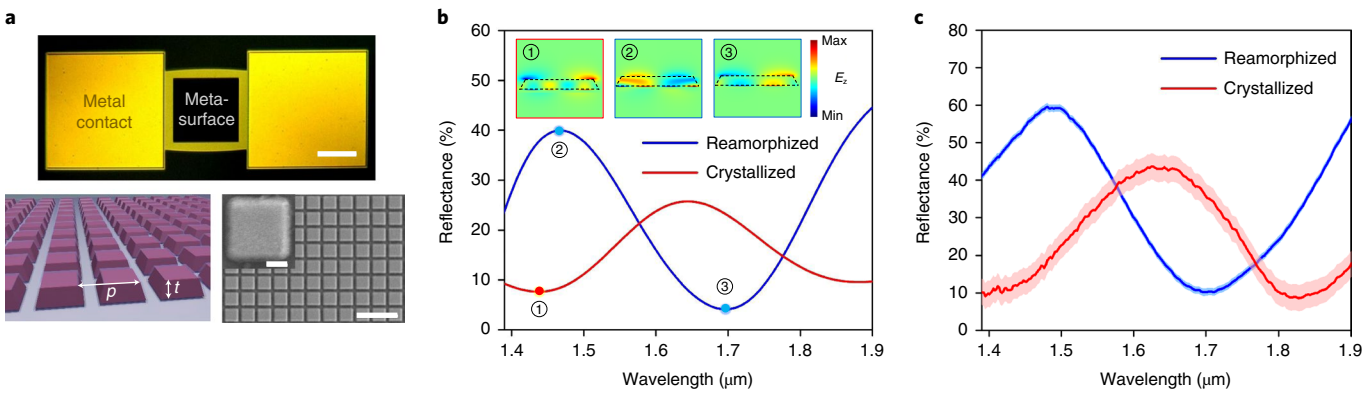

Fig. 3 | Demonstration of bi-state spectral tuning. a, Top, optical micrograph of an active metasurface device; scale bar, 100 μm; bottom, schematic and scanning electron microscopy (SEM) images showing the metasurface and (inset) a single meta atom; $p = 800$ nm, $t = 230$ nm, size of the meta atom is 620 nm; SEM scale bars are 2 μm and (inset) 200 nm. **b**, Simulated reflectance spectra of the metasurface; insets plot the electric field in the z direction in a meta atom corresponding to the three states (1–3) labelled on the spectra. **c**, Measured reflectance spectra of the metasurface. The shaded areas indicate the experimentally assessed cycle-to-cycle variations (standard deviations) up to 40 switching cycles.

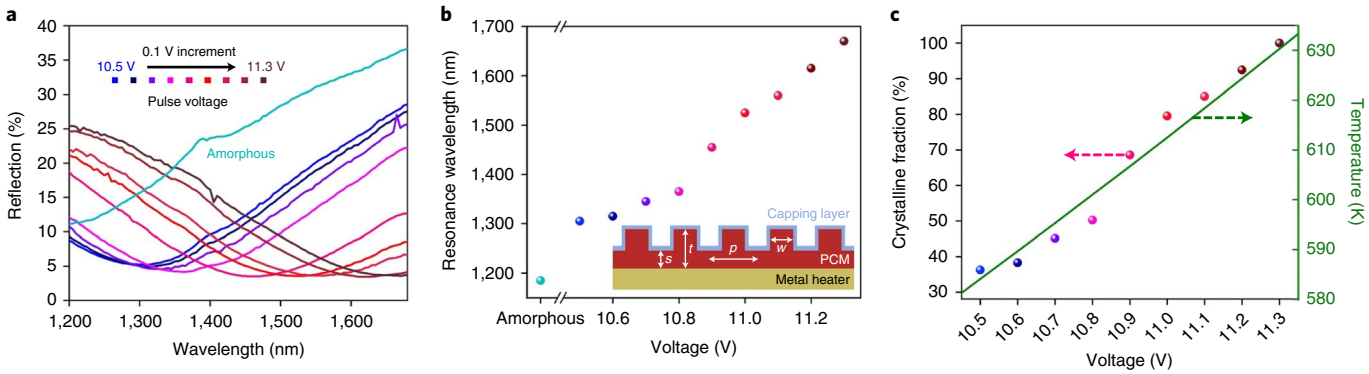

Fig. 4 | Demonstration of quasi-continuous spectral tuning. a, Reflectance spectra of the multi-state switching device after undergoing crystallization pulses with different voltages. **b**, Measured resonance wavelength as a function of the pulse voltage; inset illustrates the schematic device configuration where $t = 250$ nm, $p = 800$ nm, $s = 200$ nm and $w = 630$ nm. **c**, Volume fraction of crystalline phase associated with the different intermediate states (left axis) and the corresponding PCM temperatures during crystallization (right axis).

1.43 μm wavelength. The optical contrast is substantially larger than those achieved in active metasurfaces relying on thermo-optic or electro-optic effects[10,11] and benefits from the colossal index modification of PCMs on phase transition. The device also exhibits consistent switching characteristics with a small average cycle-to-cycle reflectance variation of 3.5% (Fig. 3c) at crystalline state and <1% at amorphous state. Further details about the metasurface design and characterization are elaborated on in Supplementary Information.

Quasi-continuous multi-state tuning

Besides the giant index modulation, PCMs are also known for their capacity for multi-state or multi-bit operation[38–41]. As discussed in the previous section, the excellent thermal uniformity inside the meta atoms indicates that the intermediate states contain interspersed crystalline and amorphous phases of varying fractions. Precise control of the phase composition of the intermediate states can be realized through either varying the crystallization electrical pulse duration or the pulse voltage, thereby regulating the crystallization kinetics. Here we choose the latter mechanism to demonstrate quasi-continuous tuning of the meta-atom resonance.

The device, which comprises meta atoms arranged in a square lattice (Fig. 4b inset), is designed to attain ultra-broadband resonance tuning. Unlike devices reported by others where the PCM layer is limited to an ultrathin (<100 nm) form factor to facilitate rapid quenching during re-amorphization and hence switching reversibility[22–25], the GSST layer in our device has a total thickness of 250 nm. Our previous work has proved that GSST exhibits improved amorphous phase stability compared to the classical GeSbTe alloys[37], which enables a much larger PCM thickness while maintaining fully reversible switching capability. The increased PCM volume affords substantially enhanced light confinement and interaction with the PCM layer, which underlies an exceptionally large resonance tuning range. Figure 4a displays reflectance spectra of the device measured after multiple crystallization cycles, where pulses with increasing voltage at 0.1 V increment were used to access different intermediate states of the PCM. Ultra-broadband tuning of the optical resonance over half an octave, from 1,190 to 1,680 nm, was measured (Fig. 4b). This is a very large spectral span that the non-mechanical active meta-optical device covers.

The result also allows quantitative evaluation of the GSST meta-atom crystallization kinetics. This is accomplished by extracting the crystalline phase fraction for each intermediate state via an effective medium theory based on the Lorentz–Lorenz equation (Fig. 4c left axis, details can be found in Supplementary Information), and correlating the pulse voltage with corresponding meta-atom temperature using finite-element modelling (Fig. 4c right axis). Our device platform therefore not only validates multi-state switching capabilities of the PCM metasurfaces but also provides a versatile platform for quantitatively assessing the crystallization kinetics of PCMs (Supplementary Information).

Beam steering using active phase-gradient Huygens' surface

Here we further show that, besides amplitude or resonance tuning, the PCM-based active metasurface platform also enables facile control of optical phase and wave front by demonstrating a polarization-insensitive reconfigurable metasurface beam deflector. The device functions as a Huygens' surface[46] consisting of only two cylindrical elements (as shown in Fig. 5g). Details of the aggressively discretized Huygens' metasurface design are furnished in Supplementary Information. Figure 5c and d presents simulated field patterns of the devices in its amorphous and crystalline states, respectively. The device is designed such that for both transverse electric and transverse magnetic polarized light at 1,550 nm wavelength normally incident on the device, the reflected beam couples to the +1 mode in the amorphous state with a deflection angle of 32° and to the 0th order mode in the crystalline state. The polarization-independent response was experimentally validated, confirming that the transverse electric and transverse magnetic deflected beams exhibit identical intensities within our measurement uncertainty. In the crystalline (amorphous) state, the measured deflection efficiency into the 0th (+1) order is 24.8% (8.3%). The switching contrast ratio, defined as $\left(I_c^0 I_a^1\right) / \left(I_c^1 I_a^0\right)$ where I represents the light intensity, the superscripts show the diffraction order and the subscripts denote the device state, was measured to be 8.6 dB, which is lower than the simulated value of 11.4 dB albeit on par with state-of-the-art active metasurface deflectors[8]. We anticipate that improved fabrication accuracy as well as adoption of advanced meta-atom designs[27,28,47] will further boost the device performance.

Conclusion

In this work, we have demonstrated an on-chip electrical switching platform enabling both binary switching and quasi-continuous tuning of PCM-based active metasurfaces. Compared to thermal or optical actuation schemes, electrical addressing of active metasurfaces represents an important step forward towards realizing fully integrated, chip-scale reconfigurable optics. In addition, we show that using a recently developed PCM, namely GSST, imparts important advantages including mitigation of optical losses and increased PCM reversible switching volume. Leveraging the enhanced light-PCM interactions, we achieved unprecedented

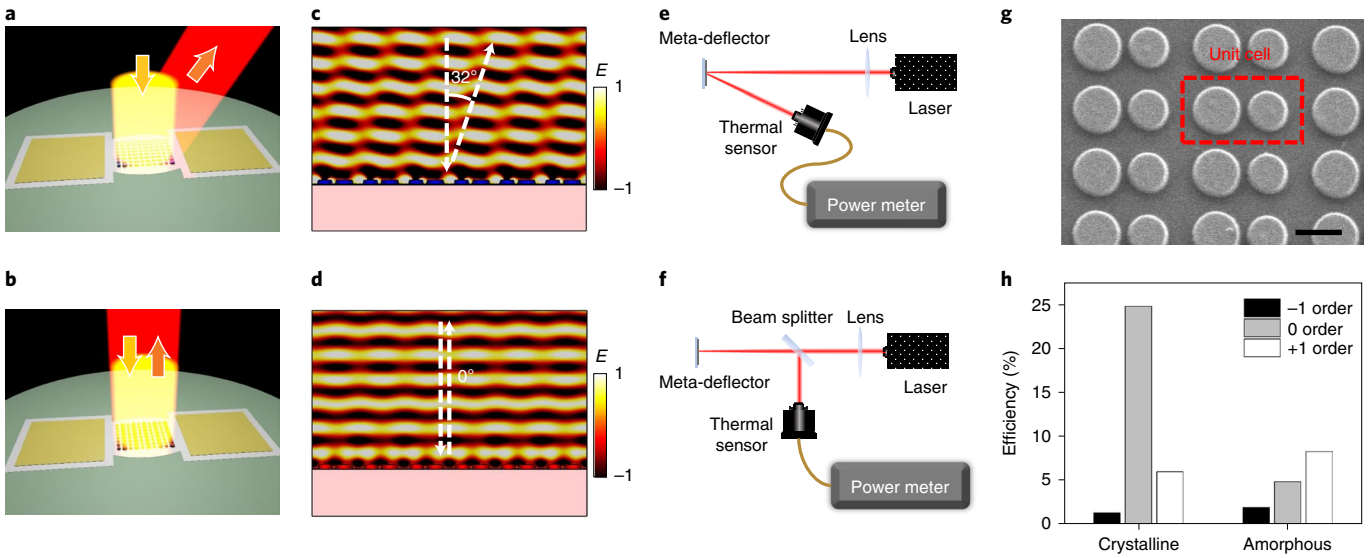

Fig. 5 | Demonstration of reconfigurable beam steering. a,**b**, Schematic rendering showing the reconfigurable metasurface beam deflector in its amorphous (**a**) and crystalline states (**b**). **c**,**d**, Simulated electric field amplitude profiles at a 1,550 nm wavelength illustrating the beam steering characteristics of the device in its amorphous (**c**) and crystalline states (**d**). **e**, Experiment setup for measuring deflection efficiencies into the ±1 orders. A thermal sensor coupled with a power metre is placed at the deflection angel. **f**, Experiment setup for measuring deflection efficiencies into the 0th order. A beam splitter is used to deflect the 0th order light to the thermal sensor. **g**, A top-view SEM image of the Huygens' surface consisting of an array of repeating unit cells. Scale bar, 1 μm. **h**, Measured deflection efficiencies of different diffraction orders at a 1,550 nm wavelength.

ultra-broadband tuning of meta-atom resonances across half an octave. This exceptionally large modulation capability is critical to realizing active metasurfaces for on-demand phase and amplitude control. As an example of phase and wave front control, we further realized active switching of a Huygens' surface beam deflector using the platform. Moreover, the electrical switching design and the geometric optimization approach for large-aperture metasurfaces demonstrated herein are also transferrable to other emerging heater materials such as silicon[48,49] and graphene[44] to enable a diverse array of reconfigurable metasurface devices.

We note that a relevant paper has been peer-reviewed at the same time as this work[50].

Online content

Any methods, additional references, Nature Research reporting summaries, source data, extended data, supplementary information, acknowledgements, peer review information; details of author contributions and competing interests; and statements of data and code availability are available at https://doi.org/10.1038/s41565-021-00881-9.

Received: 29 August 2020; Accepted: 25 February 2021;
Published online: 19 April 2021

References

1. Shaltout, A. M., Shalaev, V. M. & Brongersma, M. L. Spatiotemporal light control with active metasurfaces. *Science* **364**, eaat3100 (2019).
2. Shalaginov, M. Y. et al. Design for quality: reconfigurable flat optics based on active metasurfaces. *Nanophotonics* **9**, 3505–3534 (2020).
3. Kang, L., Jenkins, R. P. & Werner, D. H. Recent progress in active optical metasurfaces. *Adv. Opt. Mater.* **7**, 1801813 (2019).
4. Arbabi, E. et al. MEMS-tunable dielectric metasurface lens. *Nat. Commun.* **9**, 812 (2018).
5. She, A., Zhang, S., Shian, S., Clarke, D. R. & Capasso, F. Adaptive metalenses with simultaneous electrical control of focal length, astigmatism, and shift. *Sci. Adv.* **4**, eaap9957 (2018).
6. Zanotto, S. et al. Metasurface reconfiguration through lithium-ion intercalation in a transition metal oxide. *Adv. Opt. Mater.* **5**, 1600732 (2017).
7. Kafaie Shirmanesh, G., Sokhoyan, R., Pala, R. A. & Atwater, H. A. Dual-gated active metasurface at 1550 nm with wide (>300°) phase tunability. *Nano Lett.* **18**, 2957–2963 (2018).
8. Li, S. Q. et al. Phase-only transmissive spatial light modulator based on tunable dielectric metasurface. *Science* **364**, 1087–1090 (2019).
9. Ding, L. et al. Electrically and thermally tunable smooth silicon metasurfaces for broadband terahertz antireflection. *Adv. Opt. Mater.* **6**, https://doi.org/10.1002/adom.201800928 (2018).
10. Wu, P. C. et al. Dynamic beam steering with all-dielectric electro-optic III–V multiple-quantum-well metasurfaces. *Nat. Commun.* **10**, 3654 (2019).
11. Rahmani, M. et al. Reversible thermal tuning of all-dielectric metasurfaces. *Adv. Funct. Mater.* **27**, 1700580 (2017).
12. Abdollahramezani, S. et al. Tunable nanophotonics enabled by chalcogenide phase-change materials. *Nanophotonics* **9**, 1189–1241 (2020).
13. Pitchappa, P. et al. Chalcogenide phase change material for active terahertz photonics. *Adv. Mater.* **31**, 1808157 (2019).
14. Zhu, Z., Evans, P. G., Haglund, R. F. & Valentine, J. G. Dynamically reconfigurable metadevice employing nanostructured phase-change materials. *Nano Lett.* **17**, 4881–4885 (2017).
15. Kim, Y. et al. Phase modulation with electrically tunable vanadium dioxide phase-change metasurfaces. *Nano Lett.* **19**, 3961–3968 (2019).
16. Kats, M. A. et al. Thermal tuning of mid-infrared plasmonic antenna arrays using a phase change material. *Opt. Lett.* **38**, 368–370 (2013).
17. Liu, L., Kang, L., Mayer, T. S. & Werner, D. H. Hybrid metamaterials for electrically triggered multifunctional control. *Nat. Commun.* **7**, 13236 (2016).
18. Dong, W. et al. Tunable mid-infrared phase-change metasurface. *Adv. Opt. Mater.* **6**, 1701346 (2018).
19. Yin, X. et al. Beam switching and bifocal zoom lensing using active plasmonic metasurfaces. *Light.: Sci. Appl.* **6**, e17016 (2017).
20. Tian, J. et al. Active control of anapole states by structuring the phase-change alloy $Ge_2Sb_2Te_5$. *Nat. Commun.* **10**, 396 (2019).
21. Pogrebnyakov, A. V. et al. Reconfigurable near-IR metasurface based on $Ge_2Sb_2Te_5$ phase-change material. *Opt. Mater. Express* **8**, 2264 (2018).
22. Leitis, A. et al. All-dielectric programmable Huygens' metasurfaces. *Adv. Funct. Mater.* **30**, 1910259 (2020).
23. Ruiz De Galarreta, C. et al. Reconfigurable multilevel control of hybrid all-dielectric phase-change metasurfaces. *Optica* **7**, 476–484 (2020).
24. Wang, Q. et al. Optically reconfigurable metasurfaces and photonic devices based on phase change materials. *Nat. Photonics* **10**, 60–65 (2016).
25. Gholipour, B., Zhang, J., MacDonald, K. F., Hewak, D. W. & Zheludev, N. I. An all-optical, non-volatile, bidirectional, phase-change meta-switch. *Adv. Mater.* **25**, 3050–3054 (2013).
26. Wuttig, M., Bhaskaran, H. & Taubner, T. Phase-change materials for non-volatile photonic applications. *Nat. Photonics* **11**, 465–476 (2017).

27. Shalaginov, M. Y. et al. Reconfigurable all-dielectric metalens with diffraction limited performance. *Nat. Commun.* **12**, 1225 (2021).
28. An, S. et al. A deep learning approach for objective-driven all-dielectric metasurface design. *ACS Photonics* **6**, 3196–3207 (2019).
29. Cao, T. et al. Tuneable thermal emission using chalcogenide metasurface. *Adv. Opt. Mater.* **6**, 1800169 (2018).
30. Williams, C., Hong, N., Julian, M., Borg, S. & Kim, H. J. Tunable mid-wave infrared Fabry-Perot bandpass filters using phase-change GeSbTe. *Opt. Express* **28**, 10583 (2020).
31. Tittl, A. et al. A switchable mid-infrared plasmonic perfect absorber with multispectral thermal imaging capability. *Adv. Mater.* **27**, 4597–4603 (2015).
32. Carrillo, S. G.-C., Alexeev, A. M., Au, Y.-Y. & Wright, C. D. Reconfigurable phase-change meta-absorbers with on-demand quality factor control. *Opt. Express* **26**, 25567 (2018).
33. Gholipour, B., Piccinotti, D., Karvounis, A., MacDonald, K. F. & Zheludev, N. I. Reconfigurable ultraviolet and high-energy visible dielectric metamaterials. *Nano Lett.* **19**, 1643–1648 (2019).
34. Michel, A. U. et al. Advanced optical programming of individual meta-atoms beyond the effective medium approach. *Adv. Mater.* **31**, 1901033 (2019).
35. Zhang, Y. et al. Broadband transparent optical phase change materials. In *Proc. Conf. Lasers and Electro-Optics* paper JTh5C.4 (OSA Publishing, 2017); https://doi.org/10.1364/CLEO_AT.2017.JTh5C.4
36. Zhang, Q. et al. Broadband nonvolatile photonic switching based on optical phase change materials: beyond the classical figure-of-merit. *Opt. Lett.* **43**, 94 (2018).
37. Zhang, Y. et al. Broadband transparent optical phase change materials for high-performance nonvolatile photonics. *Nat. Commun.* **10**, 4279 (2019).
38. Li, X. et al. Fast and reliable storage using a 5 bit, nonvolatile photonic memory cell. *Optica* **6**, 1 (2019).
39. Rios, C. et al. Controlled switching of phase-change materials by evanescent-field coupling in integrated photonics. *Opt. Mater. Express* **8**, 2455 (2018).
40. Wu, C. et al. Low-loss integrated photonic switch using subwavelength patterned phase change material. *ACS Photonics* **6**, 87–92 (2018).
41. Zheng, J. et al. GST-on-silicon hybrid nanophotonic integrated circuits: a non-volatile quasi-continuously reprogrammable platform. *Opt. Mater. Express* **8**, 1551 (2018).
42. Lee, S.-Y. et al. Holographic image generation with a thin-film resonance caused by chalcogenide phase-change material. *Sci. Rep.* **7**, 41152 (2017).
43. Dong, W. et al. Wide bandgap phase change material tuned visible photonics. *Adv. Funct. Mater.* **29**, 1806181 (2019).
44. Ríos, C. et al. Multi-level electro-thermal switching of optical phase-change materials using graphene. *Adv. Photonics Res.* **2**, 2000034 (2021).
45. Orava, J., Greer, A. L., Gholipour, B., Hewak, D. W. & Smith, C. E. Characterization of supercooled liquid $Ge_2Sb_2Te_5$ and its crystallization by ultrafast-heating calorimetry. *Nat. Mater.* **11**, 279–283 (2012).
46. Zhang, L. et al. Ultra-thin high-efficiency mid-infrared transmissive Huygens meta-optics. *Nat. Commun.* **9**, 1481 (2018).
47. An, S. et al. Deep learning modeling approach for metasurfaces with high degrees of freedom. *Opt. Express* **28**, 31932 (2020).
48. Zheng, J. et al. Nonvolatile electrically reconfigurable integrated photonic switch enabled by a silicon PIN diode heater. *Adv. Mater.* **2001218**, 2001218 (2020).
49. Zhang, H. et al. Nonvolatile waveguide transmission tuning with electrically-driven ultra-small GST phase-change material. *Sci. Bull.* **64**, 782–789 (2019).
50. Wang, Y. et al. Electrical tuning of phase change antennas and metasurfaces. *Nat. Nanotechnol.* https://doi.org/10.1038/s41565-021-00882-8 (2020).

Methods

Material synthesis. GSST thin films were prepared using thermal evaporation from a single $Ge_2Sb_2Se_4Te$ source. Bulk starting material was synthesized using a standard melt-quench technique from high-purity (99.999%) raw elements[51]. The film deposition was performed using a custom-designed system (PVD Products, Inc.) following previously established protocols[37,52,53]. Stoichiometries of the films were confirmed using wavelength-dispersive spectroscopy on a JEOL JXA-8200 SuperProbe Electron Probe Microanalyzer to be within 2% (atomic fraction) deviation from target compositions.

Device fabrication and packaging. All the devices were fabricated on silicon wafers with 3 µm thermal oxide from Silicon Quest International. The 50 nm Ti/20 nm Pt heaters and the 10 nm Ti/100 nm Au contact pads were deposited via electron beam evaporation and patterned using lift-off. Then 10 nm of Al_2O_3 was coated using atomic layer deposition to prevent direct contact between GSST and the heater. The GSST metasurfaces were then deposited and patterned using poly(methyl methacrylate) as the electron beam lift-off resist and subsequently capped with 15 nm Al_2O_3 deposited using atomic layer deposition. All the patterning steps were carried out using electron beam lithography on an Elionix ELS-F125 system. The devices were subsequently wire bonded (using 0.8 mil 99% Al–1% Si wires) and mounted onto a custom-designed PCB, which allowed for reproducible electrical contact (as compared to using contact probes).

Optical simulation. For the multi-state metasurfaces, finite-difference time-domain simulations were performed using the commercial software package Lumerical FDTD. The periodic boundary condition was set along both x and y in-plane directions and perfectly matched layer boundary condition was used along the out-of-plane z direction. Reflectance spectra were recorded with an xy plane monitor on top of the device. For the beam deflector devices, S parameter and far-field radiation pattern calculations were carried out with the commercial full-wave computation package CST Microwave Studio using the frequency solver under unit cell boundary conditions. Optical constants for the metal heater materials and both states of GSST characterized using spectroscopic ellipsometry were used in the simulations.

Thermal simulation. The thermal simulations were performed using a three-dimensional finite-element method model constructed in COMSOL Multiphysics. A COMSOL built-in module (electric currents) was used for solving the electrical current distribution, and the heat transfer in solids module was implemented for simulating the heating transfer and temperature distribution. The two modules were coupled through the electromagnetic heat source model. In the heat transfer module, infinite element domains were adopted for the side and bottom boundaries. Convective heat flux boundary condition was used for the top surface with a heat transfer coefficient of 10 $W/(m^2 K^{-1})$. The thermal properties of GSST in the model were defined on the basis of experimentally measured data, which we will report in detail in a separate publication. Specifically, the thermal conductivity values of GSST in the model were 0.2 $W/(m K^{-1})$ for the amorphous state and 0.4 $W/(m K^{-1})$ for the crystalline state, and heat capacity values of GSST were taken as 1.45 $MJ/(m^3 K^{-1})$ for the amorphous state and 1.85 $MJ/(m^3 K^{-1})$ for the crystalline state.

Tuneable metasurface characterization. The metasurface devices with 200 µm square apertures have electrical resistances of approximately 20 Ω. To amorphize the device, a single 20 V, 5 µs pulse was applied. For crystallization, a single 500 ms pulse with a voltage of approximately 10 V was applied. A Renishaw Invia Reflex micro-Raman system was used for collecting Raman spectra on the devices. A Thermo Fisher FTIR6700 Fourier transform infrared spectrometer with an attached microscope was used to obtain the reflectance spectra of the devices. The reflectance spectra were calibrated using a standard gold mirror.

In the quasi-continuous tuning experiment, the device reflectance spectra were taken in situ using a super continuum laser (NKT Photonics SuperK Extreme Continuum Laser) with a tuneable notch filter (SuperK Select Multi-Line Tunable Filter) across the 1.2–1.7 µm spectral range, with the reflected light intensity quantified using an InGaAs short-wave infrared camera (Xenics Xeva 320 Series SWIR Camera). The reflectance spectra were similarly calibrated using a gold mirror.

Beam deflector characterization. The measurement setup was schematically illustrated in Fig. 5e,f. The device under test (DUT) was mounted on a two-dimensional translational stage for optical alignment. A laser source (LUNA Technologies OVA-5000) whose wavelength was fixed at 1,550 nm in conjunction with a fibre-optic collimator was used for characterizing the metasurface deflector. The collimated beam was focused by a lens with a 15 cm focal length onto the device. The laser beam diameter exiting from the collimator is approximately 3 mm, thereby giving rise to an effective numerical aperture of the beam of approximately 0.01. When the weakly focused beam impinged on the DUT, the spot size was 0.14 mm, which ensures that the entire spot falls on the aperture of the DUT. An infrared camera was first used to image the diffracted spots before quantifying their intensity values using a calibrated photodetector. To measure the zero-order power, a beam splitter was inserted into the optical path at 45° with respect to the optical axis. The same measurement procedure was followed as above. The total power of the laser and the transmission and reflection coefficients of all the optical components were measured to calculate the absolute reflectance of the zero order.

Data availability

The data that support the findings of this study are available from the corresponding authors upon reasonable request.

References

51. Petit, L. et al. Compositional dependence of the nonlinear refractive index of new germanium-based chalcogenide glasses. *J. Solid State Chem.* **182**, 2756–2761 (2009).
52. Hu, J. et al. Fabrication and testing of planar chalcogenide waveguide integrated microfluidic sensor. *Opt. Express* **15**, 2307 (2007).
53. Musgraves, J. D. et al. Comparison of the optical, thermal and structural properties of Ge-Sb-S thin films deposited using thermal evaporation and pulsed laser deposition techniques. *Acta Mater.* **59**, 5032–5039 (2011).

Acknowledgements

This work was funded by Defense Advanced Research Projects Agency Defense Sciences Office Program: EXTREME Optics and Imaging (EXTREME) under agreement no. HR00111720029, and by the Assistant Secretary of Defense for Research and Engineering under Air Force Contract nos. FA8721-05-C-0002 and/or FA8702-15-D-0001. We also acknowledge characterization facility support provided by the Materials Research Laboratory at Massachusetts Institute of Technology (MIT), as well as fabrication facility support by the Microsystems Technology Laboratories at MIT and Harvard University Center for Nanoscale Systems. The views, opinions and/or findings expressed are those of the authors and should not be interpreted as representing the official views or policies of the Department of Defense or the US Government. The funders had no role in study design, data collection and analysis, decision to publish or preparation of the manuscript. Any opinions, findings, conclusions or recommendations expressed in this material are those of the authors and do not necessarily reflect the views of the Assistant Secretary of Defense for Research and Engineering.

Author contributions

Y.Z. performed material deposition, device design and metasurface characterization. Y.Z. and J.L. fabricated the metasurfaces and conducted device characterization. C.F. conceived and designed the Huygens' surface. B.A., M.Y.S., S.D.-J. and C.R. assisted in device characterization. S.A. helped with device modelling. J.B.C., C.M.R. and V.L. measured the multi-state metasurfaces. M.K. prepared the bulk materials. T.G., C.R.-B., K.A.R., H.Z. and J.H. supervised the research. All authors contributed to technical discussions and writing the paper.

Competing interests

The authors declare no competing interests.

Additional information

Supplementary information The online version contains supplementary material available at https://doi.org/10.1038/s41565-021-00881-9.

Correspondence and requests for materials should be addressed to H.Z. or J.H.

Peer review information *Nature Nanotechnology* thanks Alex Krasnok, Ho Wai Howard Lee and Jinghua Teng for their contribution to the peer review of this work.

Reprints and permissions information is available at www.nature.com/reprints.